Ceramics International 51 (2025) 51912–51921

Contents lists available at ScienceDirect

Ceramics International

journal homepage: www.elsevier.com/locate/ceramint

Highly efficient and stable five-membered high-entropy spinel oxide infrared radiation coatings for application in radioisotope thermophotovoltaic systems

Zhi Yang [a], Zhiheng Xu [a,b,*], Chengxiang Wang [a], Guiying Xu [c], Yuxiong Xue [d], Xiaobin Tang [a,b,**]

[a] Department of Nuclear Science and Technology, Nanjing University of Aeronautics and Astronautics, Nanjing, 210016, China
[b] Key Laboratory of Advanced Nuclear Technology and Radiation Protection, Ministry of Industry and Information Technology, Nanjing, 211106, China
[c] Beijing Municipal Key Lab of Advanced Energy Materials and Technology, School of Materials Science and Engineering, University of Science and Technology Beijing, Beijing, 100083, China
[d] College of Electrical, Energy and Power Engineering, Yangzhou University, Yangzhou, 225127, China

ARTICLE INFO

Handling editor: P. Vincenzini

Keywords:
Radioisotope thermophotovoltaic system
High-entropy spinel oxide
Infrared radiation coating
Co-doping effect
Bandgap

ABSTRACT

The thermophotovoltaic conversion process is a pivotal energy-conversion mechanism in radioisotope thermophotovoltaic (RTPV) systems. Nevertheless, ensuring that thermal radiation materials maintain their outstanding emissive performances after extended exposure to elevated temperatures and radiation environments is a substantial challenge. In this paper, we propose the use of high-entropy spinel oxide $(Cu_{0.2}Mn_{0.2}Fe_{0.2}Cr_{0.2}Ni_{0.2})_3O_4$ coatings as infrared radiation coatings for the surfaces of radioisotope thermal sources. The synthesized coatings exhibited remarkable infrared radiation intensities that are in close approximation to those of a black body. The synergistic co-doping effect of the transition metal elements and the generation of oxygen vacancies produced a reduction in the bandgap of the material. This bandgap narrowing significantly enhances the emissive characteristics of $(Cu_{0.2}Mn_{0.2}Fe_{0.2}Cr_{0.2}Ni_{0.2})_3O_4$. After undergoing treatment at a high temperature of 1127 °C for 30 h and exposure to γ-ray irradiation with a cumulative dose of 27 kGy, the infrared emissivity of the coating remains steadfastly above 92 %. Moreover, detailed analysis revealed that there were no substantial alterations in the phase composition and microstructure of the coating. The coating enabled an RTPV system to achieve a maximum output power density of 16.63 mW/cm^2. This value represents a significant increase of 132.91 % in power density compared to the RTPV system without the coating. Therefore, this coating has potential applications in the field of efficient thermal energy utilization based on radioisotopes.

1. Introduction

Recent years have witnessed rapid advancements in the field of deep-space exploration, resulting in an increasing demand for high-reliability power supply technologies [1,2]. Consequently, the radioisotope thermophotovoltaic (RTPV) system, a nuclear power system characterized by a long lifespan and high stability, has garnered significant interest [3–5]. In this system, infrared emissive materials convert the thermal energy released from the decay of radioisotope heat sources into near-infrared photons, which are subsequently converted into electrical energy by photovoltaic cells via the photovoltaic effect. Therefore, the spectral intensity emitted by the thermal radiation materials are critical to determining the output performance and conversion efficiency of RTPV systems [6,7].

Rare-earth materials [8–10] and tungsten-based metals [11,12] are conventionally employed as emitter materials in thermophotovoltaic systems owing to their exceptional thermal stability. However, the narrow characteristic emission peaks of rare-earth materials and the intrinsically low emissivity of tungsten produce a limited overall spectral intensity, thereby constraining the output performance of TPV systems and indicating a necessity for further enhancement. Photonic crystal [13,14] and metamaterial [15,16] emitters have recently been the focal point of a significant number of research studies, as they could potentially find application in the production of RTPV systems owing to

* Corresponding author. Department of Nuclear Science and Technology, Nanjing University of Aeronautics and Astronautics, Nanjing, 210016, China.
** Corresponding author. Department of Nuclear Science and Technology, Nanjing University of Aeronautics and Astronautics, Nanjing, 210016, China.
E-mail addresses: xuzhiheng@nuaa.edu.cn (Z. Xu), tangxiaobin@nuaa.edu.cn (X. Tang).

https://doi.org/10.1016/j.ceramint.2025.08.401
Received 26 May 2025; Received in revised form 14 August 2025; Accepted 26 August 2025
Available online 27 August 2025

their good spectrally selective emission ability and high theoretical energy conversion efficiency. However, the effective application of these materials could be limited by cumbersome preparation processes and high costs. Moreover, metamaterial structures are prone to degradation under prolonged high-temperature conditions [17], and the irradiation effects induced by radioisotope heat sources are yet to be thoroughly analyzed and investigated. Therefore, it is essential to explore highly stable and efficient infrared radiation materials based on radioisotope heat sources. Spinel-type oxide materials exhibit excellent optical absorption and infrared emission properties, superior structural stability, and high-temperature resistance [18–21]. For instance, Song et al. [22] reported a $NiFe_2O_4$ spinel material with favorable radiative performance in the mid-infrared region, suitable for energy-saving applications in high-temperature industrial furnaces, and demonstrated good thermal shock resistance at 700 °C. Furthermore, the emissive properties of spinel oxides can be further enhanced by incorporating multiple transition metals to form high-entropy spinel oxides (HESO) [23–26]. Because of its inherent thermal stability and high emissivity, HESO can be used as a thermal radiation material on the surfaces of radioisotope heat sources. However, studies on the infrared radiative properties of transition-metal-doped HESO remain limited, and the emission stability after irradiation requires further investigation. Therefore, it is necessary to explore the infrared radiative behavior and stability of radioisotope heat sources under high-temperature and irradiation environments, as well as their effectiveness in enhancing the performance of RTPV systems.

In this study, a five-membered HESO $(Cu_{0.2}Mn_{0.2}Fe_{0.2}Cr_{0.2}Ni_{0.2})_3O_4$ was synthesized via a high-temperature solid-phase method and investigated as a thermal-radiation-coating material for radioisotope heat sources. A systematic study was conducted to analyze the influence of different solid-phase reaction temperatures on material properties during the preparation process. The high-temperature infrared spectral intensity of the coating was measured, and the infrared thermography temperatures at various temperature gradients were determined. These data were compared with those of tungsten and alumina emitters, which are more conventionally used. Furthermore, the infrared emission mechanism of $(Cu_{0.2}Mn_{0.2}Fe_{0.2}Cr_{0.2}Ni_{0.2})_3O_4$ was elucidated by analyzing bandgap variations. To verify the emission stability of the coating, long-term high-temperature and radiation-irradiation experiments were performed. The coating was applied to the surface of an electrically heated alumina heat source and integrated into an RTPV system. The performance output effects at different heat-source temperatures were experimentally evaluated. The results demonstrated that the coating exhibited excellent infrared emission properties and structural stability under long-term high-temperature and high-irradiation environments when used on the surfaces of radioisotope heat sources. The design of the coating contributes to the simplification and miniaturization of the RTPV system, indicating its great potential for applications in long-life space nuclear power systems.

2. Materials and methods

2.1. Preparation of the $(Cu_{0.2}Mn_{0.2}Fe_{0.2}Cr_{0.2}Ni_{0.2})_3O_4$ powder and coating

Fig. 1 illustrates the $(Cu_{0.2}Mn_{0.2}Fe_{0.2}Cr_{0.2}Ni_{0.2})_3O_4$ coating preparation process. Equal metal atom molar ratios of CuO (99.5 % purity), NiO (99.5 % purity), MnO_2 (99.5 % purity), Fe_2O_3 (99.5 % purity), and Cr_2O_3 (99.5 % purity) powders were weighed. The weighed powders were then mixed with anhydrous ethanol and zirconia milling balls in a mass ratio of 1:3:4 in a ball-milling jar, followed by ball milling at 500 rpm for 8 h to obtain a uniform slurry. Subsequently, the homogeneous slurry was dried in a blast drying oven at 80 °C for 24 h and ground to form a precursor powder. The powder was poured into an alumina crucible and placed in a tube furnace and calcined for 5 h at 700 °C, 800 °C, 900 °C, and 1000 °C, respectively, with a temperature increase rate of 5 °C/min, so that the metal oxide powder underwent a solid-phase reaction to form a spinel structure at high temperatures. After cooling to room temperature with the furnace, the resulting sample was ground in a mortar to obtain $(Cu_{0.2}Mn_{0.2}Fe_{0.2}Cr_{0.2}Ni_{0.2})_3O_4$ powder. The powder, ethyl cellulose, rosinol solvent, and inorganic silicate binder were mixed at a mass ratio of 1:0.03:0.72:0.03, followed by ball milling at a rotational speed of 300 rpm for 5 h to obtain a uniform coating slurry.

The surfaces of radioisotope heat sources are typically covered with ceramic oxide materials containing alumina. Therefore, alumina was

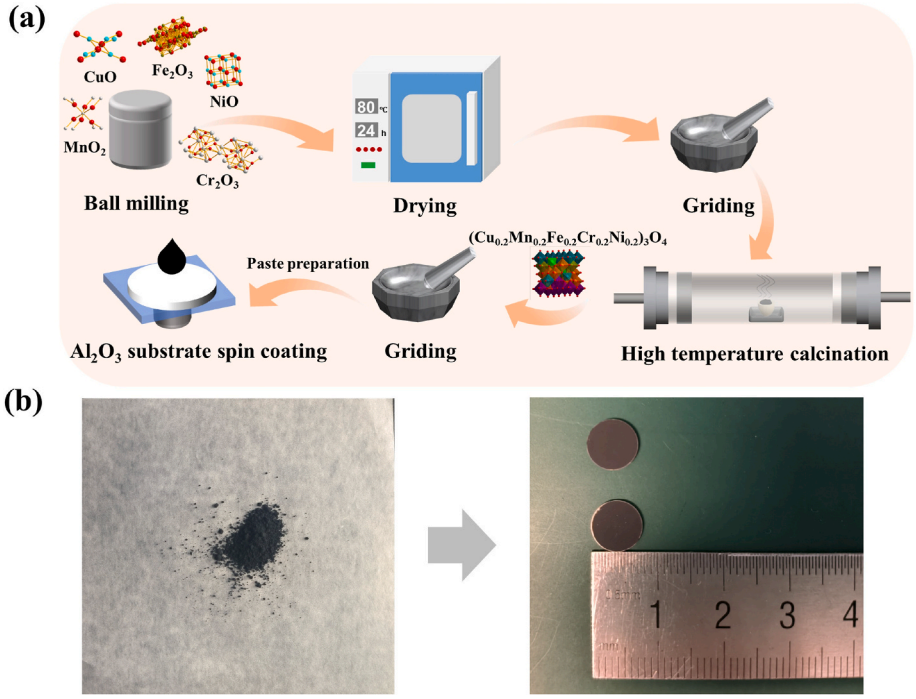

Fig. 1. (a) Coating preparation process, (b) prepared powder and coating.

selected as the substrate material for the coating, and metallic tungsten, a typical thermal radiation material, was used as the reference sample. Circular alumina substrates (diameter: 8 mm, thickness: 1 mm) were immersed in anhydrous ethanol for ultrasonic cleaning to ensure surface purity. The prepared slurry was then dropped onto the surface of the alumina substrates and spin coated at 2500 rpm for 30 s. After spin coating, the samples were left to stand at room temperature for 4 h, followed by drying in an oven at 90 °C for 2 h. Subsequently, the samples were annealed for 2 h in a tubular furnace under an inert gas atmosphere at the corresponding sintering temperature (700 °C, 800 °C, 900 °C, and 1000 °C), resulting in $(Cu_{0.2}Mn_{0.2}Fe_{0.2}Cr_{0.2}Ni_{0.2})_3O_4$ coatings. The annealing process is primarily intended to eliminate organic components such as binders, thereby preventing any potential impact on the emissivity of the coating. Moreover, it promotes a stronger physical adhesion between the coating and the substrate. In addition, to enable an experimental evaluation within the RTPV system, the coating was applied to electrically heated rods that served as equivalent heat sources. After the cylindrical heat-source rods were ultrasonically cleaned in anhydrous ethanol to remove surface contaminants, the $(Cu_{0.2}Mn_{0.2}Fe_{0.2}Cr_{0.2}Ni_{0.2})_3O_4$ slurry was uniformly applied to the surfaces using a coating machine. The subsequent processing steps were carried out according to the procedure described above.

2.2. Performance testing and characterization of the powder and coating

X-ray diffraction (XRD) analysis of the $(Cu_{0.2}Mn_{0.2}Fe_{0.2}Cr_{0.2}Ni_{0.2})_3O_4$ powder and the coated samples was performed using an Empyrean X-ray diffractometer. The surface morphologies of the materials were characterized using a LYRA3 GM ionizing dual-beam electron microscope. X-ray photoelectron spectroscopy (XPS) was performed using an ESCALAB X-ray photoelectron spectrometer. The reflectance $R(\lambda)$ and absorbance A of the coatings at room temperature were obtained by testing with a LAMBDA 1050+ UV–Vis NIR spectrophotometer. According to Kirchhoff's law (Eq. (1)), the emissivity of an object at thermal equilibrium $\varepsilon(\lambda)$ is equal to the absorptivity $\alpha(\lambda)$ at the same wavelength. Therefore, the emissivity of an object can be derived indirectly by calculating its reflectance $R(\lambda)$ and transmittance $T(\lambda)$. And in the case of coatings with large thicknesses, the transmittance $T(\lambda)$ can be considered to be equal to 0.

$$\varepsilon(\lambda) = \alpha(\lambda) = 1 - R(\lambda) - T(\lambda) \quad (1)$$

The coating and reference samples were heated to 1027 °C using a RT-1300GP high-temperature heating stage at a heating rate of 50 °C/min. The infrared radiation spectra of the materials were recorded using an NIR2500 near-infrared spectrometer (Shanghai Fuxiang Optical Co., Ltd.). Additionally, a cryogenic heating stage was employed to heat the samples to three temperature gradients of 300 °C, 350 °C, and 400 °C, during which the infrared distribution images of the materials were captured using an ST9450 infrared thermal imaging camera.

2.3. High-temperature and irradiation resistance testing of the coating

To evaluate the service stability of the coatings, the prepared coating samples were subjected to high-temperature treatment in a muffle furnace at 1127 °C for 30 h, after which they were cooled to room temperature. To further assess the thermal shock resistance of the coating, thermal cycling tests from 25 °C to 1000 °C were performed using dual-temperature-zone transfer method. The sample was held for 5 min at each temperature zone, with a total of 60 cycles. Meanwhile, the coated heating rod samples were directly heated to 1000 °C, maintained for 5 min, and then rapidly cooled to room temperature, also for 60 cycles. In addition, equivalent radiation experiments were conducted at the ^{60}Co irradiation center of Nanjing University of Aeronautics and Astronautics. The samples were continuously exposed to a γ-radiation field with a dose rate of 270 Gy/h for 100 h. Based on the reported surface dose rate of 0.135 Gy/h for a general-purpose heat source using $^{238}PuO_2$ fuel core blocks [27], this corresponds to an equivalent operational duration of approximately 22.8 years.

2.4. The electrical performance testing of the RTPV system

A schematic of the RTPV system, in which an electrically heated equivalent heat source was used to simulate a radioisotope heat source for experimental investigation, is presented in Fig. 2. The surface of the heating rod was coated with $(Cu_{0.2}Mn_{0.2}Fe_{0.2}Cr_{0.2}Ni_{0.2})_3O_4$ paint. Power to the heating rod was supplied by a DPS305U high-precision switching DC power supply, with the heat source temperature set in the range of 427–727 °C. Temperature measurements of the heat source were recorded using an AS887 four-channel thermocouple thermometer. To mitigate the thermal accumulation caused by nonconvertible infrared photons, a one-dimensional SiO_2/TiO_2 optical filter was utilized to achieve selective spectral control in the infrared region. The transmission spectrum of the filter is shown in Fig. S1. An InGaAs TPV cell with a bandgap of 0.72 eV was employed for photovoltaic conversion, and the external quantum efficiency (EQE) of the TPV cell was meticulously measured using a QE-R3011 tester. The electrical output performance of the RTPV was comprehensively characterized using a Keithley 4200 SCS Characteristic Parameter Analyzer.

3. Results and discussion

3.1. Analysis of characterization results

Fig. 3 shows the XRD patterns of $(Cu_{0.2}Mn_{0.2}Fe_{0.2}Cr_{0.2}Ni_{0.2})_3O_4$ powders synthesized at various solid-state reaction temperatures. The diffraction peaks observed in the samples correspond well with those of standard spinel-structured Fe_3O_4 (PDF No. 75–0449), indicating that solid-state reactions among the mixed metal oxides occurred at elevated temperatures, leading to the formation of a spinel phase. However, the crystallinity of the powders varied at different solid-phase temperatures, and from the XRD results, the diffraction peaks were of lower intensity at the reaction temperature of 700 °C, and there might be an incomplete reaction. With increasing temperature, the (311) diffraction peaks of $(Cu_{0.2}Mn_{0.2}Fe_{0.2}Cr_{0.2}Ni_{0.2})_3O_4$ gradually narrowed, the peak intensity increased, and the peak position had a tendency to be slightly shifted to the left, which indicated that the crystallinity of the powders increased when the reaction temperature increased.

Fig. 4 presents the morphology of the powders calcined at different temperatures. At 700 °C, the spinel polyhedral outlines are indistinct. As the temperature increases to 800 °C and 900 °C, the crystallinity improves and grain interfaces become more pronounced. Notably, powders calcined at 900 °C exhibit well-defined polyhedral shapes, indicating a more complete reaction. However, at 1000 °C, significant grain agglomeration occurs due to the formation of large grains, which may reduce the specific surface area and thereby weaken the effective interaction between the material surface and incident infrared radiation. Furthermore, excessive grain growth tends to increase surface smoothness, diminishing multiple scattering effects and adversely affecting the coating's light-absorption and thermo-optical characteristics. On a macroscopic level, these changes diminish the material's thermal emissivity. Fig. 5 shows the emissivity of coatings prepared at different solid-state reaction temperatures. The coatings prepared at reaction temperatures of 700 °C and 800 °C exhibit varying degrees of emissivity reduction due to incomplete reactions. Furthermore, compared with the coating obtained at 900 °C, the coating prepared at 1000 °C shows a slight decrease in emissivity in the wavelength range beyond approximately 1400 nm. This result further confirms that grain growth and agglomeration at high temperatures can affect the infrared radiation performance of the coating. Based on the above analysis, this work selects the grain coating with a reaction temperature of 900 °C as the first object to be considered in subsequent research.

Fig. 6 shows the morphological characteristics of the

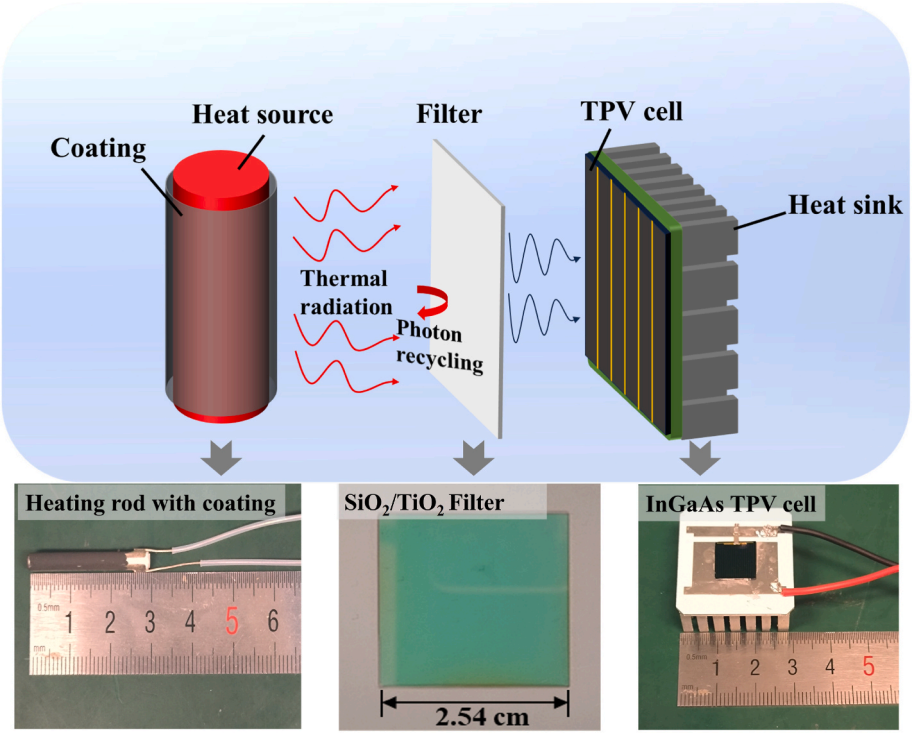

Fig. 2. Schematic diagram of the RTPV system.

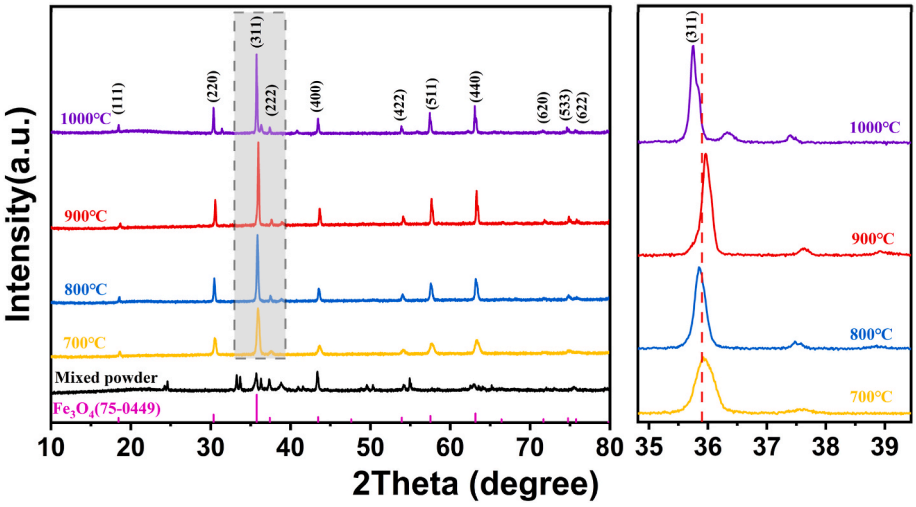

Fig. 3. XRD spectra of $(Cu_{0.2}Mn_{0.2}Fe_{0.2}Cr_{0.2}Ni_{0.2})_3O_4$ powders at different calcination temperatures.

$(Cu_{0.2}Mn_{0.2}Fe_{0.2}Cr_{0.2}Ni_{0.2})_3O_4$ powders before and after calcination. The mixed oxide powders before the reaction consisted of irregular agglomerated particles, and after calcination, the powders mainly exhibited irregular polyhedral agglomerations and smooth crystalline surfaces. The elemental mapping of the powders (Fig. S2) revealed a uniform distribution of metals and oxygen, which is consistent with the typical features of high-entropy spinel oxide materials. Moreover, the elemental mapping of the powder sample synthesized at 1000 °C reveals a uniform distribution of all metal elements (Fig. S3), with no evident signs of elemental enrichment or depletion. This indicates that under the current synthesis conditions, all elements were effectively incorporated into the spinel lattice without noticeable volatilization or phase separation. The thickness of the coating prepared using the spin-coating method was approximately 24.20 μm (Fig. S4). In addition, the XRD characterization results and surface morphology images of the coatings obtained after spin coating and subsequent calcination at the corresponding temperatures (Fig. S5) indicate that the high-temperature annealing process did not affect the spinel phase.

3.2. Analysis of infrared radiation performance and mechanism

Fig. 7 shows the emissivity of the three emitter materials in the range of 300–1800 nm at room temperature and the response bands of the InGaAs TPV cell. In particular, the average emissivity of the coating was maintained above 92 %, whereas the emissivity of the commonly used tungsten metal emitter gradually decreased from 60 % to approximately 20 %. Compared to the other two materials, the emissivity of the $(Cu_{0.2}Mn_{0.2}Fe_{0.2}Cr_{0.2}Ni_{0.2})_3O_4$ coating was more competitive in the response range of the InGaAs TPV components.

It can also be observed from the radiation spectra plots of the three

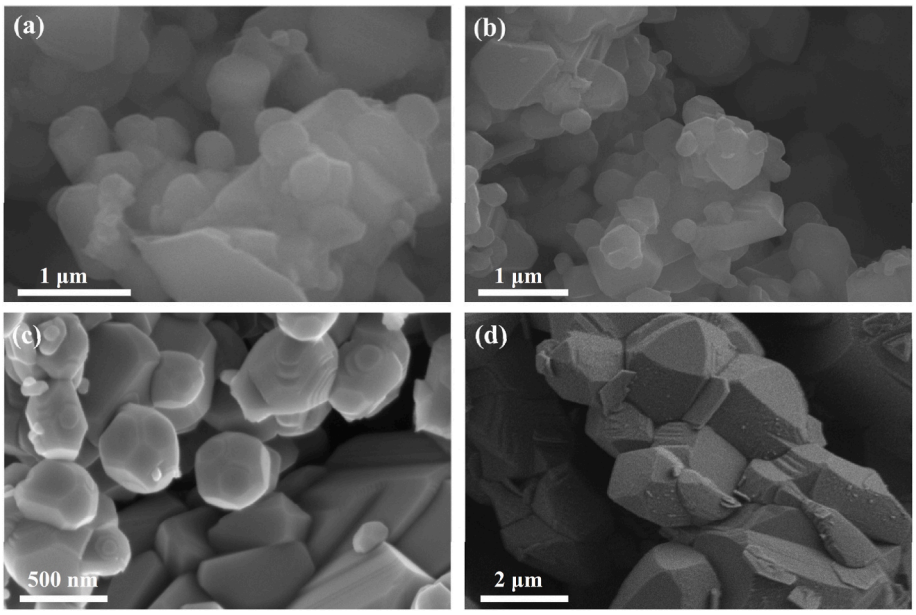

Fig. 4. Morphological images of $(Cu_{0.2}Mn_{0.2}Fe_{0.2}Cr_{0.2}Ni_{0.2})_3O_4$ powders calcined at different temperatures: (a) 700 °C, (b) 800 °C, (c) 900 °C, and (d) 1000 °C.

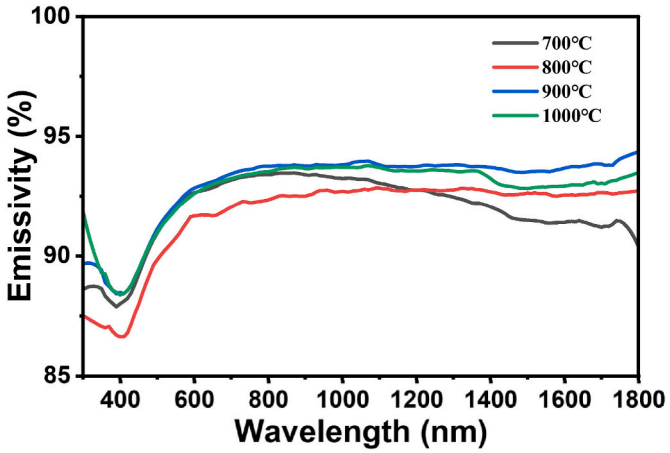

Fig. 5. Emissivity of coatings prepared at different solid-state reaction temperatures.

materials at 1027 °C (Fig. 8a) that the $(Cu_{0.2}Mn_{0.2}Fe_{0.2}Cr_{0.2}Ni_{0.2})_3O_4$ coating has a spectral power density closer to that of a blackbody. Compared with the other two thermal emitter materials, the coating provided more light intensity gain (yellow part) in the response interval of the TPV assembly. Under thermal equilibrium conditions, the radiation captured by an infrared imaging system primarily depends on the infrared emissivity of the material. Infrared imaging results at different temperature gradients (Fig. 8b) revealed that the $(Cu_{0.2}Mn_{0.2}Fe_{0.2}Cr_{0.2}Ni_{0.2})_3O_4$ coating exhibited a higher surface temperature, indicating that the coating also demonstrated efficient radiative heat transfer in the mid-to low-temperature range. Furthermore, as the temperature increased, the temperature gradient became more pronounced, and the brightness of the coated region in the captured infrared images gradually intensifies (Fig. S6), which corresponded to an increased amount of radiative energy being transferred.

The full XPS spectra of the $(Cu_{0.2}Mn_{0.2}Fe_{0.2}Cr_{0.2}Ni_{0.2})_3O_4$ elements (Fig. 9a) further confirm the presence of the incorporated metal elements and oxygen, with the 2p orbitals of the metal elements exhibiting peak splitting. As shown in Fig. 9b, for Cu as an example, the Cu $2p_{3/2}$ characteristic peaks located at 931.01 eV and 934.10 eV correspond to Cu^+ and Cu^{2+}, respectively, while the Cu $2p_{1/2}$ characteristic peaks at 951.19 eV and 954.07 eV correspond to Cu^+ and Cu^{2+} [28,29], respectively. Two satellite peaks at 941.65 eV and 961.40 eV can be attributed to Cu^{2+}. In addition, other metal elements exhibited valence state changes (Fig. S7). The Mn $2p_{3/2}$ split peaks indicate the coexistence of Mn^{3+} and Mn^{4+}. The Ni 2p spectral splitting reveals the presence of both Ni^{2+} and Ni^{3+}. For Fe, the characteristic Fe 2p peaks along with the corresponding satellite features suggest the coexistence of Fe^{2+} and Fe^{3+}. Similarly, the Cr 2p split peaks correspond to Cr^{3+} and Cr^{6+} oxidation states. The general chemical formula for spinels is AB_2O_4, where the A-site is an octahedral void coordinated by four oxygen atoms, typically occupied by divalent or low-valent cations, and the B-site is an octahedral void coordinated by six oxygen atoms, usually occupied by trivalent or higher-valent cations. Based on the XPS spectra, along with the chemical characteristics and site occupancy preferences of the constituent elements, it can be inferred that Cu^{2+}, Cu^+, Ni^{2+}, and Fe^{2+} primarily occupy the A-sites (tetrahedral positions) in the spinel structure, whereas Cr^{3+}, Cr^{6+}, Mn^{3+}, Mn^{4+}, Ni^{3+}, and Fe^{3+} are more likely to reside in the B-sites (octahedral positions). Moreover, the O 1s spectrum (Fig. 9c) shows three characteristic peaks at 530.05 eV, 530.89 eV, and 531.7 eV, which are attributed to lattice oxygen (O_L), oxygen vacancies (O_V), and adsorbed oxygen (O_A), respectively.

The high-emission mechanism of $(Cu_{0.2}Mn_{0.2}Fe_{0.2}Cr_{0.2}Ni_{0.2})_3O_4$ is related to changes in its band gap. During high-temperature calcination, the doping of multiple metal cations leads to a local charge imbalance, and the difference in bond energies and lengths between the metal cations and lattice oxygen rebalances the electrons around the lattice oxygen, leading to a shift in the position of the metal ions, which results in lattice distortion [30]. Lattice distortion allows oxygen ions to escape from the lattice, thereby forming oxygen vacancies. Oxygen vacancies can introduce defect energy levels, which can effectively promote the transfer of electrons and improve the light absorption performance at infrared wavelengths [31]. The material bandgap was calculated from the experimentally measured absorbance data using Tauc's formula (Eq. (2)):

$$(\alpha h\nu)^n = C(h\nu - E_g) \tag{2}$$

where $h\nu$ is the photon energy, E_g is the optical band gap of the material of interest, C is an energy-independent constant, and α is the absorption coefficient. Based on the Beer–Lambert law, a proportional relationship

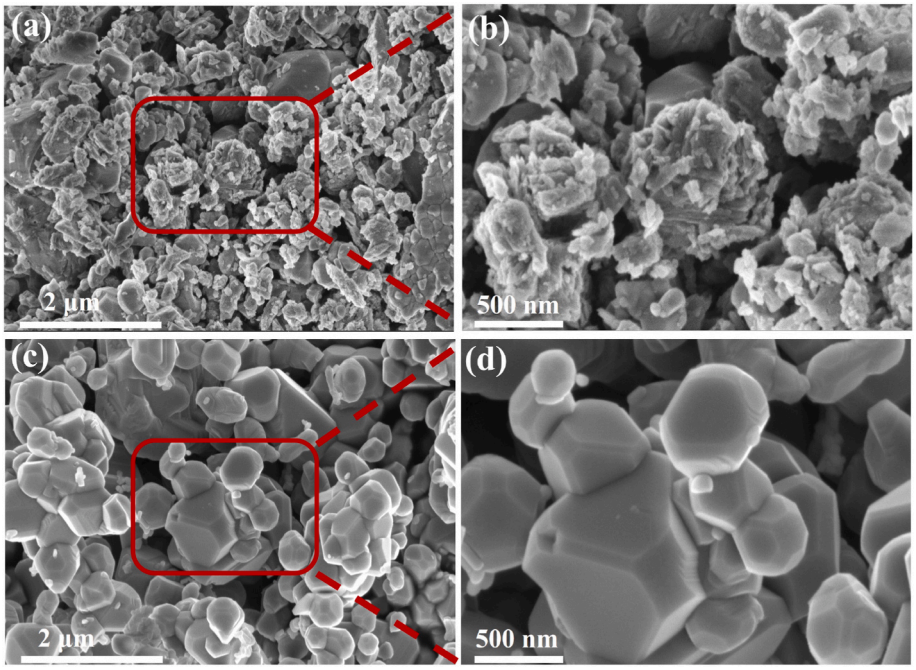

Fig. 6. (a)–(b) SEM images of mixed oxide powders before calcination. (c)–(d) SEM images of $(Cu_{0.2}Mn_{0.2}Fe_{0.2}Cr_{0.2}Ni_{0.2})_3O_4$ powder with a reaction temperature of 900 °C.

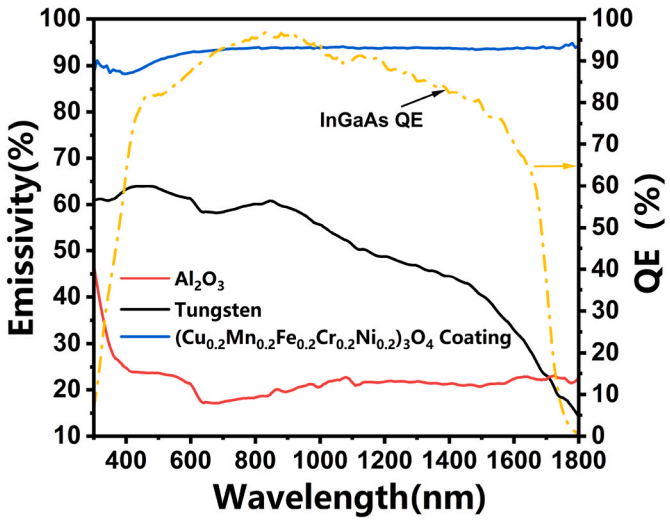

Fig. 7. Emissivity of three thermal emitter materials and the external quantum efficiency of the InGaAs TPV cell.

exists between absorbance and the absorption coefficient:

$$A = K\alpha \tag{3}$$

where A is the absorbance of the sample and K is a constant independent of the absorption coefficient. Therefore, the Tauc equation can be reasonably rewritten in the form:

$$(Ahv)^n = T(hv - E_g) \tag{4}$$

In this equation, T is a constant independent of photon energy. The exponent n is taken as two for direct bandgap jumps and 0.5 for indirect jumps. It was shown that a direct bandgap exists in spinel ceramic compounds [32], and the value of the bandgap energy was calculated by extrapolating the linearly fitted region at $(Ahv)^n$ with respect to the photon energy. Fig. 10 shows the fitting results for the bandgap of the material. Compared to the conventional spinel ferrite material [21], $(Cu_{0.2}Mn_{0.2}Fe_{0.2}Cr_{0.2}Ni_{0.2})_3O_4$ formed by transition metal doping has a narrower band gap and improved light absorption properties.

The synergistic effect of transition-metal co-doping and the presence of oxygen vacancies as lattice defects resulted in the formation of impurity energy levels within the bandgap, effectively narrowing the bandgap of the material. This facilitates enhanced electronic transitions of the outermost d-orbital electrons of transition metals, leading to improved infrared absorption [33]. Therefore, the bandgap narrowing is primarily attributed to the increased concentration of oxygen vacancies induced by the high-entropy effect. According to Kirchhoff's law, under thermal equilibrium conditions, an increase in infrared absorption within the same wavelength range promotes a corresponding enhancement in infrared emissivity. This enables HESO materials to exhibit spectral intensities approaching that of an ideal blackbody. In RTPV systems, this characteristic primarily translates to an increased flux of useable photons received by the photovoltaic conversion unit.

3.3. High-temperature and irradiation stability analysis of HESO coating

Owing to the unique environment of the radioisotope heat source, the coating must maintain a stable emissivity even after prolonged exposure to high temperatures and radiation. Fig. 11 shows the emissivity curves of the coating after 30 h of high-temperature treatment at 1127 °C and irradiation at a total dose of 27 kGy from a ^{60}Co source. It can be observed that after high-temperature treatment, the emissivity of the coating does not exhibit a significant decrease, with only a slight reduction occurring beyond 1200 nm. After irradiation, the emissivity of the $(Cu_{0.2}Mn_{0.2}Fe_{0.2}Cr_{0.2}Ni_{0.2})_3O_4$ coating exhibited a minimal decrease of less than 1 %, indicating that the coating retained excellent intrinsic stability.

Fig. 12(a) and (b) show the microscopic morphology of the coating after two different treatments. After the high-temperature treatment, the spinel polyhedral structure remained intact, while the grain size increased, which was reflected in the shift of the X-ray diffraction peaks to lower angles. According to the X-ray diffraction results (Fig. 12c), the phase composition of the coating remained unchanged after both the high-temperature and ionizing radiation treatments. Compared with the

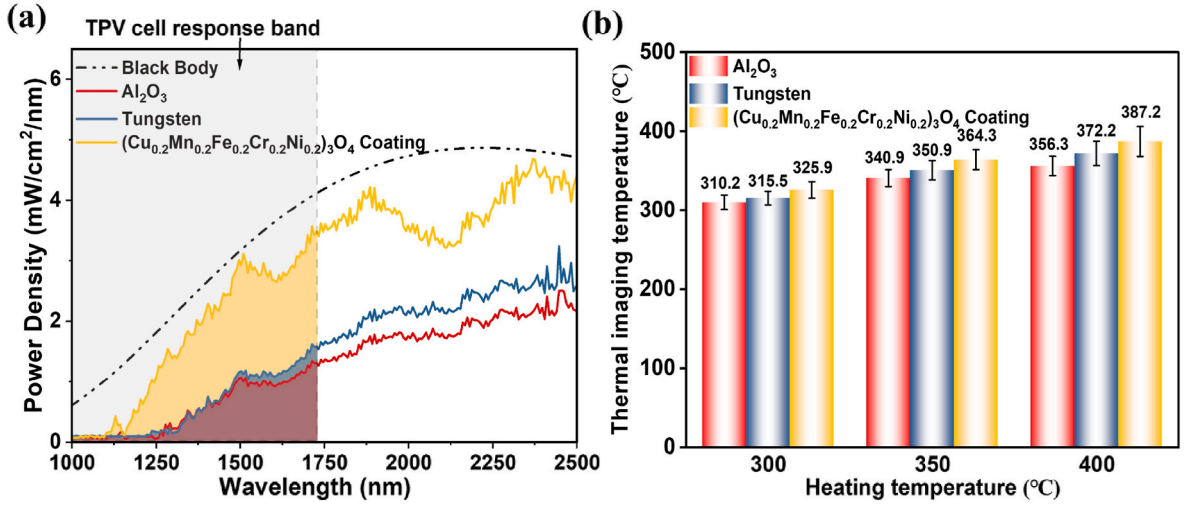

Fig. 8. (a) Infrared spectra of different emitter materials at 1027 °C. (b) Surface imaging temperatures under different thermal gradients.

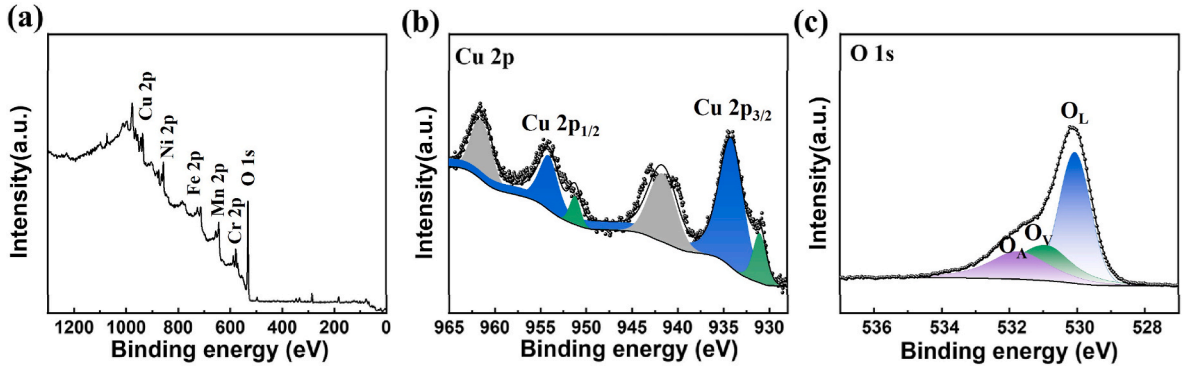

Fig. 9. (a) XPS full spectrum of $(Cu_{0.2}Mn_{0.2}Fe_{0.2}Cr_{0.2}Ni_{0.2})_3O_4$ powder, XPS spectrum of (b) Cu element and (c) O element.

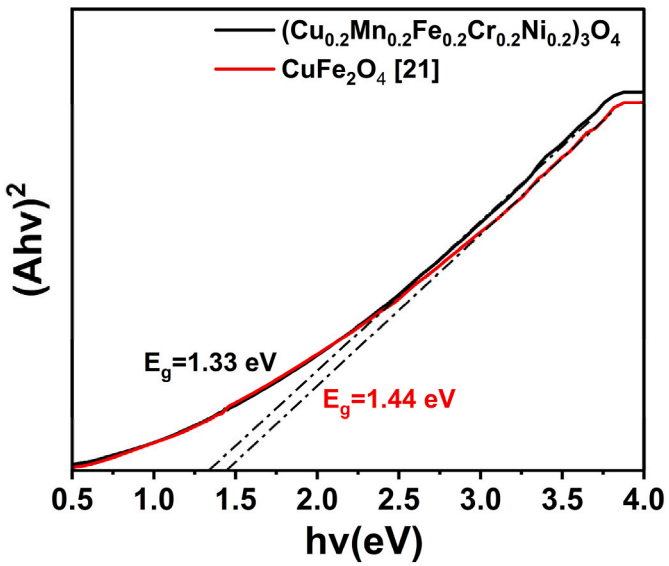

Fig. 10. Results of band gap fitting of $(Cu_{0.2}Mn_{0.2}Fe_{0.2}Cr_{0.2}Ni_{0.2})_3O_4$ and $CuFe_2O_4$ spinel.

original sample (Fig. 12d), the increase in grain size at high temperatures led to the aggregation of larger grains, resulting in a decrease in the specific surface area for light absorption, which in turn affected the optical absorption capability and caused a slight decrease in the emissivity beyond 1200 nm. After irradiation, the coated grains retained their polyhedral structures. Additionally, the elemental composition and content analyses (Table S1) indicated that the metal atoms still adhered to the molar ratio requirements. Small bubble-like projections appeared on the surface of the polyhedral grains owing to the accumulation of internal defects after prolonged irradiation, which resulted in a phase transition from spinel to disordered spinel. However, oxygen Frenkel pair defects introduced by doping with transition metal atoms can increase the radiation resistance of the spinel structure [34], which is an advantage of the high-entropy effect.

Fig. 13 shows the surface morphology of the coatings before and after thermal cycling. As observed, the overall macroscopic morphology of the coating remained largely unchanged after 60 thermal shock cycles, with no visible cracks or delamination. Furthermore, the coating on the surface of the heating rod exhibited no noticeable changes and remained well adhered to the substrate. These results further demonstrate the excellent thermal stability of the coating.

3.4. Electrical properties of the HESO-coating based RTPV system

Fig. 14 presents the current-voltage (*I-V*) and power density-voltage (*P-V*) curves of the RTPV system equipped with a coated heat source and a standard Al_2O_3 heat source at various temperatures. Application of the coating led to a significant enhancement in both the output current density and power density of the RTPV system. This improvement was attributed to the markedly increased infrared spectral intensity of the coating at the same temperature, resulting in a higher flux of useable

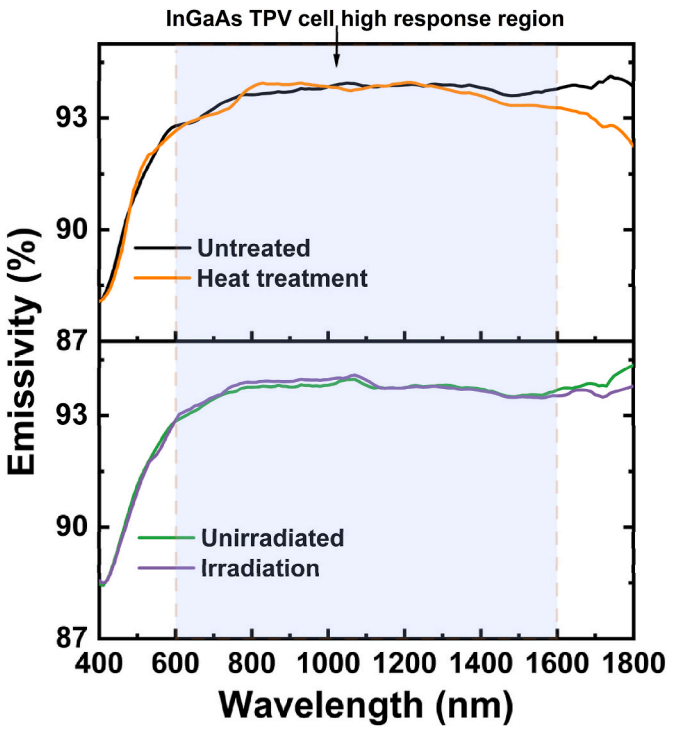

Fig. 11. Comparison of emissivity of coatings after high temperature and ionizing radiation treatment.

infrared photons and, consequently, a substantial increase in the output current. The electrical parameters of the RTPV system at different heat source temperatures were summarized in Table 1. At a heat-source temperature of 727 °C, the RTPV system with the coating achieved a short-circuit current density (J_{sc}) of 30.09 mA/cm^2 and a maximum power density (P_{max}) of 16.63 mW/cm^2. Compared to the RTPV system employing an Al_2O_3-based heat source, J_{sc} exhibited an increase of 76.58 %, whereas P_{max} was enhanced by 132.91 %.

In addition, the enhanced radiative intensity introduced by the coating led to a moderate increase in the open-circuit voltage (V_{oc}), although the extent of this enhancement was relatively limited. Because of the spectral selectivity of the optical filter, the application of the coating did not result in additional thermal loading on the TPV cell. The cell temperature remained stable without a significant increase, and no decline in V_{oc} was observed with increasing heat-source temperature. These results confirm that the integration of the $(Cu_{0.2}Mn_{0.2}Fe_{0.2}Cr_{0.2}Ni_{0.2})_3O_4$ coating into RTPV systems can substantially enhance the overall output performance.

4. Conclusion

In this study, a HESO $(Cu_{0.2}Mn_{0.2}Fe_{0.2}Cr_{0.2}Ni_{0.2})_3O_4$ coating was successfully synthesized and demonstrated excellent emissive characteristics. The infrared radiative intensity of the as-prepared coating approached that of an ideal blackbody. The synergistic effect of co-doping with multiple transition metal elements and the presence of oxygen vacancies within lattice defects lead to the formation of a narrow bandgap, which is the key factor enabling the high emissivity of the coating. Even after undergoing high-temperature treatment at 1127 °C and exposure to γ-ray irradiation with a cumulative dose of 27 kGy, the coating maintains remarkable structural and functional stability. Specifically, no substantial alterations were detected in the spinel-phase structure or surface morphology. Elemental distribution analysis revealed that the elements within the coating remained uniformly dispersed, and the metal content consistently adhered to the equimolar ratio. When integrated into an RTPV system, the coating exhibited excellent performance, achieved a short-circuit current density of 30.09 mA/cm^2 and a maximum output power density of 16.63 mW/cm^2. Compared to the RTPV system without the HESO coating, J_{sc} increased by 76.58 %, and the power density improved by 132.91 %. The coating developed in this study not only simplified the structural design of the RTPV system but also significantly enhanced its output performance. Moreover, owing to its superior optical absorption and radiative heat

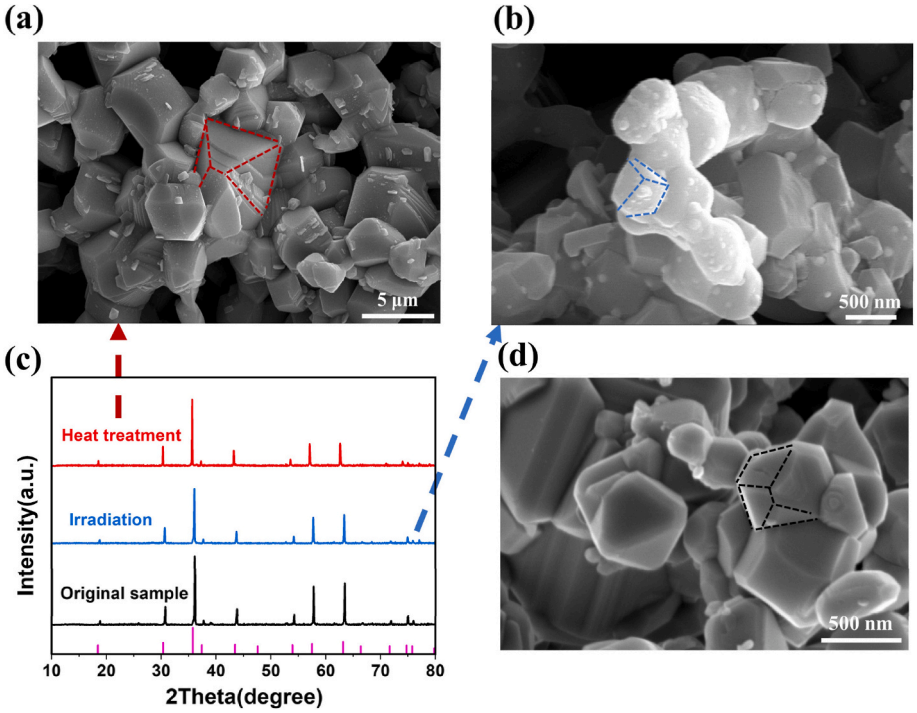

Fig. 12. Surface microstructure of the coating (a) after high-temperature treatment, (b) after irradiation treatment, and (d) original sample. (c) XRD spectra of the coating after different treatment.

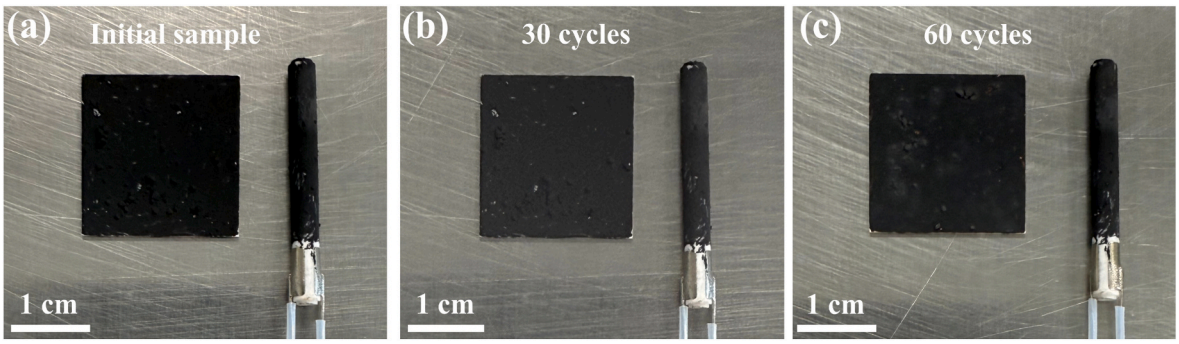

Fig. 13. Macroscopic morphology of the coating (a) before thermal cycling, (b) after 30 thermal cycles, and (c) after 60 thermal cycles.

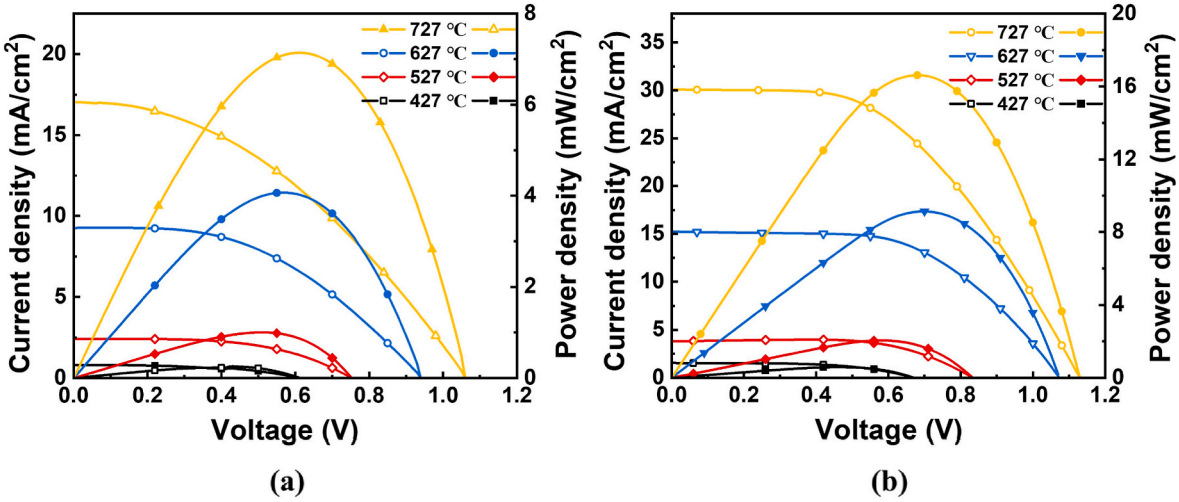

Fig. 14. *I-V/P-V* curves of the RTPV systems: (a) before and (b) after HESO coating.

Table 1
Performance parameters of RTPV systems before and after HESO coating.

Temperature (°C)	Before HESO coating				After HESO coating			
	J_{sc} (mA/cm^2)	V_{oc} (V)	P_{max} (mW/cm^2)	TPV cell temperature (°C)	J_{sc} (mA/cm^2)	V_{oc} (V)	P_{max} (mW/cm^2)	TPV cell temperature (°C)
427	0.812	0.61	0.231	24.1	1.543	0.67	0.589	25.5
527	2.417	0.75	1.005	27.2	3.792	0.83	2.049	28.8
627	9.262	0.94	4.069	30.7	15.229	1.07	9.131	31.3
727	17.045	1.06	7.142	36.2	30.091	1.13	16.626	37.8

transfer properties, the coating holds great promise for potential applications in solar energy harvesting technologies and protection of high-temperature devices.

CRediT authorship contribution statement

Zhi Yang: Writing – original draft, Methodology, Formal analysis, Data curation. **Zhiheng Xu:** Writing – review & editing, Supervision, Methodology, Funding acquisition, Conceptualization. **Chengxiang Wang:** Methodology, Investigation. **Guiying Xu:** Writing – review & editing. **Yuxiong Xue:** Writing – review & editing. **Xiaobin Tang:** Writing – review & editing, Supervision, Methodology.

Declaration of competing interest

The authors declare that they have no known competing financial interests or personal relationships that could have appeared to influence the work reported in this paper.

Acknowledgements

We acknowledge the Center for Microscopy and Analysis at Nanjing University of Aeronautics and Astronautics for structural characterization of materials. This work was supported by the National Natural Science Foundation of China (Grant No. 12275132), and the prospective layout project of Nanjing University of Aeronautics and Astronautics (Grant No. ILB240161A24).

Appendix A. Supplementary data

Supplementary data to this article can be found online at https://doi.org/10.1016/j.ceramint.2025.08.401.

References

[1] G. Schmidt, L. Dudzinski, T. Sutliff, Radioisotope power: a key technology for deep space exploration, 6th Int Energy Convers Eng Conf (IECEC). (2008) 5640, https://doi.org/10.2514/6.2008-5640.

[2] D. Wilt, D. Chubb, D. Wolford, P. Magari, C. Crowley, Thermophotovoltaics for space power applications, AIP Conf. Proc. 890 (2007) 335–345, https://doi.org/10.1063/1.2711751.
[3] P. Bermel, M. Ghebrebrhan, W. Chan, Y.X. Yeng, M. Araghchini, R. Hamam, C. H. Marton, K.F. Jensen, M. Soljačić, J.D. Joannopoulos, S.G. Johnson, I. Celanovic, Design and global optimization of high-efficiency thermophotovoltaic systems, Opt. Express 18 (2010) A314–A334, https://doi.org/10.1364/OE.18.00A314.
[4] J. Wang, X. Tang, S. Zhao, H. Deng, C. Ji, H. Wang, Y. Liu, X. Li, H. Lu, Z. Xu, An efficient photon utilization radioisotope thermophotovoltaic based on curled reflectors, Energy Technol. 11 (2023) 2201477, https://doi.org/10.1002/ente.202201477.
[5] H. Wang, Z. Xu, C. Wang, Z. Hou, M. Bian, N. Zhuang, H. Tao, Y. Wang, X. Tang, Optimized design and application performance analysis of heat recovery hybrid system for radioisotope thermophotovoltaic based on thermoelectric heat dissipation, Appl. Energy 355 (2024) 122259, https://doi.org/10.1016/j.apenergy.2023.122259.
[6] C.J. Crowley, Thermophotovoltaic converter performance for radioisotope power systems, AIP Conf. Proc. 746 (2005) 601–614, https://doi.org/10.1063/1.1867178.
[7] Y. Bian, Z. Wang, D. Tian, B. Huang, S. Liu, S. Su, S. Zhang, C. Han, X. Chen, A. Yang, J. Shao, Design and simulation of a milliwatt-level radioisotope thermophotovoltaic system, Case Stud. Therm. Eng. 63 (2024) 105378, https://doi.org/10.1016/j.csite.2024.105378.
[8] N. Nakagawa, H. Ohtsubo, Y. Waku, H. Yugami, Thermal emission properties of $Al_2O_3/Er_3Al_5O_{12}$ eutectic ceramics, J. Eur. Ceram. Soc. 25 (2005) 1285–1291, https://doi.org/10.1016/j.jeurceramsoc.2005.01.031.
[9] C. Meng, Y. Liu, Z. Xu, H. Wang, X. Tang, Selective emitter with core–shell nanosphere structure for thermophotovoltaic systems, Energy 239 (2022) 121884, https://doi.org/10.1016/j.energy.2021.121884.
[10] Z. Hou, H. Wang, J. Wang, Y. Liu, X. Tang, K.A.A. Gamage, Z. Xu, Core–shell structure selective emitter doped with rare earth elements for solar thermophotovoltaic system, Sol. Energy 264 (2023) 112081, https://doi.org/10.1016/j.solener.2023.112081.
[11] M. Danaeifar, M.A. Shameli, S.R. Mirnaziry, A selective tungsten emitter with a nearly flat configuration for thermophotovoltaic applications, Int Conf Technol Energy Manag (ICTEM). (2024) 1–3, https://doi.org/10.1109/ICTEM60690.2024.10631967.
[12] M. Chirumamilla, G.V. Krishnamurthy, S.S. Rout, M. Ritter, M. Störmer, A. Y. Petrov, M. Eich, Thermal stability of tungsten based metamaterial emitter under medium vacuum and inert gas conditions, Sci. Rep. 10 (2020) 3605, https://doi.org/10.1038/s41598-020-60419-2.
[13] F. Chen, X. Liu, Y. Liu, Y. Tian, Y. Zheng, A refractory metal-based photonic narrowband emitter for thermophotovoltaic energy conversion, J. Mater. Chem. C 11 (2023) 1988–1994, https://doi.org/10.1039/D2TC04644J.
[14] S. Cao, Q. Cai, Y. Zhang, Q. Zhang, Q. Ye, W. Deng, X. Wu, Emission mechanism and wide-angle adaptability of selective emitter based on combination of one and two-dimensional photonic crystals, Front. Energy Res. 10 (2023) 995782, https://doi.org/10.3389/fenrg.2022.995782.
[15] K. Yuan, B. Chen, S. Shan, J. Xu, Q. Yang, Tunable narrowband metamaterial thermophotovoltaic emitter: ideal performance analysis and structural design based on photovoltaic cell performance matching, Energy Convers. Manag. 312 (2024) 118556, https://doi.org/10.1016/j.enconman.2024.118556.
[16] X. Liu, C. Zhao, B. Wang, J. Xu, Tailorable bandgap-dependent selective emitters for thermophotovoltaic systems, Int. J. Heat Mass Tran. 200 (2023) 123504, https://doi.org/10.1016/j.ijheatmasstransfer.2022.123504.
[17] T. Cai, Z. Xu, Y. Yi, C. Wang, B. Zhou, C. Chen, Y. Liu, Y. Wang, H. Lu, X. Tang, Advancing thermal radiation efficiency with hybrid-patterned metasurface emitters in thermophotovoltaic systems, Int. J. Therm. Sci. 213 (2025) 109790, https://doi.org/10.1016/j.ijthermalsci.2025.109790.
[18] P. Ma, Q. Geng, X. Gao, S. Yang, G. Liu, Solution combustion of spinel $CuMn_2O_4$ ceramic pigments for thickness sensitive spectrally selective (TSSS) paint coatings, Ceram. Int. 42 (2016) 11966–11973, https://doi.org/10.1016/j.ceramint.2016.04.122.
[19] L. Hou, F. Ge, Y. Niu, C. Yuan, Efficient fabrication of spinel copper ferrite with enhanced high infrared radiation properties, Ceram. Int. 46 (2020) 21166–21171, https://doi.org/10.1016/j.ceramint.2020.05.194.
[20] E.Y. Sako, H.D. Orsolini, M. Moreira, D. De Sousa Meneses, V.C. Pandolfelli, Emissivity of spinel and titanate structures aiming at the development of industrial high-temperature ceramic coatings, J. Eur. Ceram. Soc. 41 (2021) 2958–2967, https://doi.org/10.1016/j.jeurceramsoc.2020.11.010.
[21] H. Wang, Z. Xu, Z. Yuan, K. Liu, C. Meng, X. Tang, High-temperature and radiation-resistant spinel-type ferrite coating for thermo-optical conversion in radioisotope thermophotovoltaic generators, Energy 239 (2022) 122255, https://doi.org/10.1016/j.energy.2021.122255.
[22] X. Song, S. Zhu, Z. Ma, L. Liu, W. Leng, Y. He, Preparation of infrared high radiation coatings from modified spinel $NiFe_2O_4$ and its energy saving applications, Ceram. Int. 48 (2022) 20362–20371, https://doi.org/10.1016/j.ceramint.2022.03.320.
[23] B. Liu, C. He, Y. Li, Z. Li, W. Wang, Z. Lu, Z. Wang, S. Zhao, G. Liu, X. Gao, Quasi-metallic high-entropy spinel oxides for full-spectrum solar energy harvesting, Matter 7 (2024) 140–157, https://doi.org/10.1016/j.matt.2023.10.020.
[24] Q. Wan, F. Zhang, Y. Xiong, New spinel-structured high-entropy oxides with high- and stable-infrared radiation properties, J. Am. Ceram. Soc. 107 (2024) 4747–4756, https://doi.org/10.1111/jace.19760.
[25] W. Wang, B. Liu, C. He, P. Zhao, S. Zhao, Z. Wang, Z. Lu, H. Guo, G. Ren, G. Liu, X. Gao, High-entropy engineering for broadband infrared radiation, Adv. Funct. Mater. 33 (2023) 2303197, https://doi.org/10.1002/adfm.202303197.
[26] X. Zeng, Z. Liu, X. Tong, Y. Xiong, C. Hu, J. Bian, X. Cheng, Q. Cao, Preparation and infrared emissivity of metal borides(metal=V,Mo,Fe) and MnO_2 co-doped $NiCr_2O_4$ coatings, Ceram. Int. 48 (2022) 5581–5589, https://doi.org/10.1016/j.ceramint.2021.11.102.
[27] S.J. Cheon, S.G. Hong, J.H. Lee, Y.S. Nam, Design and performance analysis of a 500-W heat source for radioisotope thermophotovoltaic converters, Int. J. Energy Res. 42 (2018) 817–829, https://doi.org/10.1002/er.3889.
[28] Y. Gao, B. Li, Z. Zhang, X. Zhang, Z. Deng, L. Huo, S. Gao, $CuMn_2O_4$ spinel nanoflakes for amperometric detection of hydrogen peroxide, ACS Appl. Nano Mater. 4 (2021) 6832–6843, https://doi.org/10.1021/acsanm.1c00898.
[29] J. Patra, T.X. Nguyen, C.C. Tsai, O. Clemens, J. Li, P. Pal, W.K. Chan, C.H. Lee, H.Y. T. Chen, J.M. Ting, J.K. Chang, Effects of elemental modulation on phase purity and electrochemical properties of Co-free high-entropy spinel oxide anodes for lithium-ion batteries, Adv. Funct. Mater. 32 (2022) 2110992, https://doi.org/10.1002/adfm.202110992.
[30] H. Guo, W. Wang, C. He, B. Liu, D. Yu, G. Liu, X. Gao, Entropy-assisted high-entropy oxide with a spinel structure toward high-temperature infrared radiation materials, ACS Appl. Mater. Interfaces 14 (2021) 1950–1960, https://doi.org/10.1021/acsami.1c20055.
[31] Z. Xi, X. Aday, M. Dong, B. Liu, C. He, G. Ren, X. Gao, Enhanced broadband infrared radiation from rare earth orthochromites for high-temperature radiative heat transfer, Chem. Eng. J. 497 (2024) 154905, https://doi.org/10.1016/j.cej.2024.154905.
[32] R. Mguedla, A. Ben Jazia Kharrat, M. Saadi, K. Khirouni, N. Chniba Boudjada, W. Boujelben, Structural, electrical, dielectric and optical properties of $PrCrO_3$ ortho-chromite, J. Alloys Compd. 812 (2020) 152130, https://doi.org/10.1016/j.jallcom.2019.152130.
[33] C. He, Y. Li, Z. Zhou, B. Liu, X. Gao, High-entropy photothermal materials, Adv. Mater. 36 (2024) 2400920, https://doi.org/10.1002/adma.202400920.
[34] C. Liu, Y. Li, T. Shi, Q. Peng, F. Gao, Oxygen defects stabilize the crystal structure of $MgAl_2O_4$ spinel under irradiation, J. Nucl. Mater. 527 (2019) 151830, https://doi.org/10.1016/j.jnucmat.2019.151830.